Monitoring brain temperature by time-resolved near-infrared spectroscopy: pilot study

Mohammad Fazel Bakhsheshi
Mamadou Diop
Keith St. Lawrence
Ting-Yim Lee

Monitoring brain temperature by time-resolved near-infrared spectroscopy: pilot study

Mohammad Fazel Bakhsheshi,[a,b,c,*] Mamadou Diop,[a,c] Keith St. Lawrence,[a,b,c] and Ting-Yim Lee[a,b,c]
[a]Lawson Health Research Institute, Imaging Program, London, Ontario N6A 4V2, Canada
[b]Robarts Research Institute, Imaging Research Laboratories, London, Ontario N6A 5B7, Canada
[c]Western University, Department of Medical Biophysics, London, Ontario N6A 3K7, Canada

Abstract. Mild hypothermia ($HT_{32°C-33°C}$) is an effective neuroprotective strategy for a variety of acute brain injuries. However, the wide clinical adaptation of $HT_{32-33°C}$ has been hampered by the lack of a reliable non-invasive method for measuring brain temperature, since core measurements have been shown to not always reflect brain temperature. The goal of this work was to develop a noninvasive optical technique for measuring brain temperature that exploits both the temperature dependency of water absorption and the high concentration of water in brain (80%–90%). Specifically, we demonstrate the potential of time-resolved near-infrared spectroscopy (TR-NIRS) to measure temperature in tissue-mimicking phantoms (*in vitro*) and deep brain tissue (*in vivo*) during heating and cooling, respectively. For deep brain tissue temperature monitoring, experiments were conducted on newborn piglets wherein hypothermia was induced by gradual whole body cooling. Brain temperature was concomitantly measured by TR-NIRS and a thermocouple probe implanted in the brain. Our proposed TR-NIRS method was able to measure the temperature of tissue-mimicking phantoms and brain tissues with a correlation of 0.82 and 0.66 to temperature measured with a thermometer, respectively. The mean difference between the TR-NIRS and thermometer measurements was 0.15°C ± 1.1°C for the *in vitro* experiments and 0.5°C ± 1.6°C for the *in vivo* measurements. © *2014 Society of Photo-Optical Instrumentation Engineers (SPIE)* [DOI: 10.1117/1.JBO.19.5.057005]

Keywords: brain temperature; time-resolved near-infrared spectroscopy; absorption coefficient; reduced scattering coefficient; piglet.

Paper 140089R received Feb. 14, 2014; revised manuscript received Apr. 6, 2014; accepted for publication Apr. 8, 2014; published online May 9, 2014.

1 Introduction

Clinical studies have shown that hypothermia improves neurological outcome and reduces mortality following cardiac arrest, traumatic brain injury, birth asphyxia, and ischemic encephalopathy.[1–3] Despite its well-documented efficacy, the widespread application of hypothermia in neuroemergencies has been hampered by the difficulty to noninvasively monitor brain temperature.[4,5] As well, cooling the whole body below 33°C–34°C can induce severe complications, including sclerema, skin erythema, renal failure, coagulopathy, pulmonary hypertension, and even death.[6] Selective brain cooling (SBC) methods, such as the use of a cooling helmet or nasopharyngeal cooling, have been proposed to alleviate the complications associated with systemic hypothermia by directly cooling the brain while maintaining body temperature as close to normal as possible.[7] However, SBC requires a method that can measure local brain temperature rather than body temperature because the latter may not reflect the actual brain temperature.[8]

Several approaches have been developed to assess brain temperature. Temperature can be measured invasively by inserting a thermometer directly into the brain parenchyma, which provides accurate measurements but carries a significant risk of complications. Infrared tympanic thermometer is noninvasive; however, it is not convenient for continuous monitoring and is sensitive to positioning errors.[9–12] Magnetic resonance spectroscopy can be used to measure brain temperature,[13] but its clinical utility is hampered by long measurement time and the need to transfer patients to imaging facilities. Temperature measurement techniques have also been developed using other modalities, such as ultrasound,[14] microwave radiometry,[15] and the zero heat flux technique.[16] However, these techniques suffer from practical issues, such as inducing an increase in brain temperature during its operation,[14,17] and poor temporal or spatial resolution.[18,19]

Optical methods are a promising alterative to the aforementioned techniques since they are safe and the instruments are compact and portable. As well, temperature-dependent changes in water absorption spectra have been well characterized by near-infrared spectroscopy (NIRS).[20] The water absorption peaks around 740, 840, and 970 nm shift to shorter wavelengths and increase in intensity with increasing temperature[20–22] due to decreases in the extent of intermolecular hydrogen bonding among water molecules as temperature increases. In fact, NIRS thermometry approaches based on broadband continuous wave (CW) and diffuse optical spectroscopy have been developed to predict deep tissue temperature in the adult forearm and breast, respectively.[20,23] Chung et al. used the water peak at 970 nm to predict temperature in tissue-mimicking phantoms and breast tissue.[23] Using this water peak to monitor brain temperature is challenging because of the strong water absorption at this wavelength, which limits depth penetration. In this report, the temperature dependency of the water absorption peaks at 740 and 840 nm was investigated as an alternative approach for monitoring brain temperature. Although the temperature-dependent

*Address all correspondence to: Mohammad Fazel Bakhsheshi, Email: mfazelba@uwo.ca

changes at these features are not as great as at 970 nm, this is compensated for by the increased penetration depth at these wavelengths. Time-resolved NIRS (TR-NIRS) was used in order to separate the effects of tissue scattering from absorption and to provide better depth sensitivity.[24] The method was validated in tissue-mimicking phantoms by correlating TR-NIRS temperature calculations to simultaneous thermometer measurements, and subsequently used to monitor brain temperature in newborn piglets during cooling. Deep brain temperature was also measured continuously with a thermocouple probe in the *in vivo* experiments.

2 Materials and Methods

2.1 *Instrumentation*

The light sources of the TR-NIRS system consisted of thermo-electrically cooled picosecond pulsed diode lasers (LDH-P-C, PicoQuant, Germany) emitting at 760, 810, and 830 nm and a computer-controlled laser driver (SEPIA PDL 828, PicoQuant, Germany). These emission wavelengths were chosen to quantify tissue chromophores (oxy-hemoglobin, HbO_2, and deoxy-hemoglobin, Hb)[25] and characterize temperature-dependent changes associated with water absorption.[20] The lasers' output power and pulse repetition rate were set to 1.4 mW and $\sim$27 MHz, respectively. The individual pulses of the three lasers were temporally separated by sharing the 80-MHz clock of the laser driver. Light emitted by each laser was attenuated by two adjustable neutral density filters (NDC-50-4M, Thorlabs, Newton, New Jersey) and coupled by a microscope objective lens (NA = 0.25, magnification = 10× into one arm of a trifur-cated fiber bundle (three fibers; NA = 0.22, core 400 μm, Fiber Optics Technology, Pomfret, Connecticut). The distal common end of the bundle (emission probe) was placed on the surface of the phantom (or scalp of the piglets) and held in position by a probe holder. The average power delivered to a subject was attenuated by the aforementioned neutral density filters to $\sim$20 μW per laser, which is below American National Standards Institute (ANSI) safety limits for skin exposure.[26]

Photons emerging from the phantom or the piglet scalp were collected by a 2-m fiber optic bundle (detection probe: NA = 0.55, 3.6-mm diameter active area, and 4.7-mm outer diameter,

fiber optics technology). The other end of the detection probe was secured in front of an electromechanical shutter (SM05, Thorlabs). Light transmitted through the shutter was collected by a Peltier cooled microchannel plate photomultiplier tube (PMC-100, Becker and Hickl, Germany) in which output was transmitted to a time-correlated single-photon counting module (SPC-134, Becker and Hickl, Germany) to build the temporal point spread function (TPSF). A schematic diagram of the TR-NIRS system and the experimental setup of the tissue mim-icking phantom are shown in Fig. 1.

2.2 *Optical Properties Measurement*

To quantify tissue optical properties (i.e., the absorption coeffi-cient μ_a and the reduced scattering coefficient μ_s' from the mea-sured TPSFs, the instrument response function (IRF) was measured to account for temporal dispersion in the system.[27] The IRF was acquired by placing a thin piece of white paper between the emission fiber and the detection fiber bundles. The paper was coated with black toner to reduce specular reflec-tion.[28] IRFs were measured at the start and end of each experi-ment at the same count rate as the TPSFs. The optical properties were obtained using an analytical model of light diffusion.[29] The model solution was first convolved with the measured IRF, and then a nonlinear optimization routine (based on the MATLAB® function fminsearch) was used to fit the convolved model to each measured TPSF to determine μ_a, μ_s', and a scaling factor that accounts for variations in laser power, drifts in the intensity of light source, detection gain, and coupling efficiency.[27] The fitting range was set to 80% of the peak value on the leading edge and 20% on the falling edge.[30] The TPSFs measured at baseline (i.e., before initiation of cooling) were averaged and fitted to extract the baseline optical properties as well as the scal-ing factor. Thereafter, changes in light absorption caused by cooling were characterized by μ_a, with μ_s' and the scaling factor set to their baseline values. This approach improves the stability of the fitting procedure and reduces errors caused by cross talk between fitting parameters.[20,27] Potential temperature effects on μ_i' were evaluated by repeating the fitting procedure with both μ_a and μ_s' as fitting parameters. Tissue optical properties at each temperature were determined by averaging 32 TPSFs collected
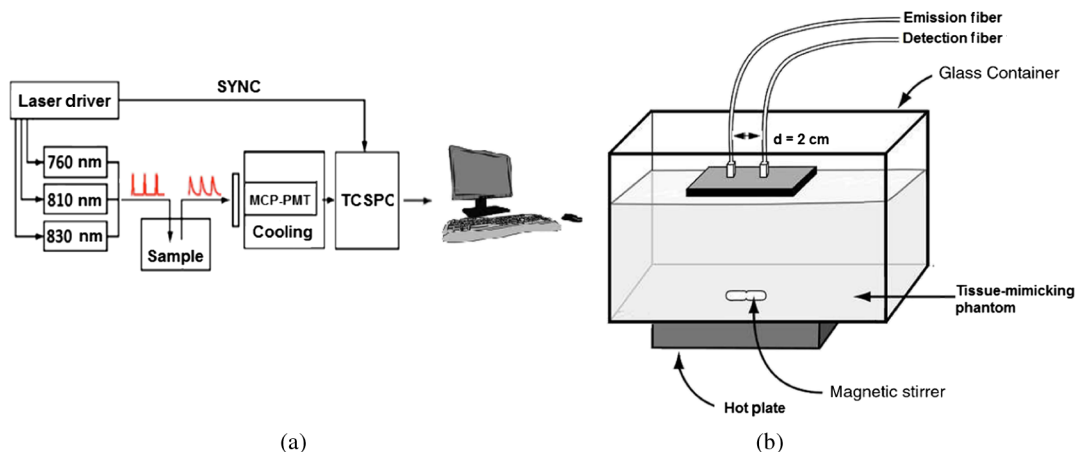

<center>(a)</center>

<center>(b)</center>

Fig. 1 (a) Schematic of the time-resolved (TR) system. Light emitted by each diode laser was coupled into one arm of a trifurcated emission fiber bundle. (b) Setup of the tissue-mimicking phantom experi-ments. The phantom solution was contained in a glass container placed on a heated and stirring plate. The emission and detector probes of the TR instrument were positioned on the surface of the solution at a source-detector distance of 2 cm.

over 320 s. The maximum count rate was set to 1% of the laser repetition rate to minimize pile-up effect.[31] Finally, the measured changes in μ_a were used to calculate changes in temperature, as discussed in detail in Sec. 3.1.

2.3 Tissue-Mimicking Phantom Experiments

Tissue-mimicking phantoms ($N = 7$), composed of 95% distilled water, 0.8% intralipid, and 4.2% whole piglet blood, were used for comparison of TR-NIRS temperature calculations and thermometer measurements. The solution was contained in a Pyrex beaker and placed on a heated stirring plate and covered with a light-tight blanket to reduce background signal contamination. The emission and detector probes of the TR-NIRS instrument were positioned on the surface of the solution at a source-detector distance of 2 cm. A thermometer (VWR digital thermometer with 0.1°C precision, VWR International Inc., Canada) was also placed in the solution for concomitant TR-NIRS and temperature measurements. The phantom solution was stirred with a magnetic stirrer before each measurement to ensure homogeneity of the optical properties and temperature. Each experiment was completed within 3 h during which the sample temperature was raised from ~32°C to 38°C. The phantom and its container were weighed prior to heating, and again at the end of the experiment. The average total weight loss during the whole experiment was ~0.5 ± 0.3%.

2.4 Animal Preparation and Experimental Procedure

In vivo experiments were conducted on eight piglets (6 females and 2 males) whose average age and weight were 1.6 ± 0.7 days and 1.9 ± 0.4 kg, respectively. The experiments were approved by the Animal Use Subcommittee of the Canadian Council on Animal Care at Western University. Newborn Duroc cross piglets were obtained from a local supplier on the morning of the experiment. Piglets were anesthetized with 1%–2% isoflurane (3%–4% during preparatory surgery). A tracheotomy was performed and the piglet was ventilated with a volume-controlled mechanical ventilator to deliver a mixture of oxygen and medical air (2∶1). A femoral artery was catheterized to monitor heart rate (HR) and mean arterial blood pressure (MAP), and to intermittently collect arterial blood samples for gas analysis and measurement of blood glucose levels. Deep brain temperature was also measured continuously with a thermocouple probe. For this purpose, a burr hole was drilled in the skull with a Dremal tool and the needle thermocouple probe was inserted laterally through the skull into the brain to a depth of 2 cm vertical from the brain surface and 1.5 cm posterior to the bregma along the midline. After surgery, a heated water blanket was used to maintain rectal temperature between 37.5°C and 38.5°C. Normocapnia (37–40 mmHg) was also maintained throughout the experiment by adjusting the breathing rate and volume, depending on the arterial CO_2 tension (pCO_2) obtained from the blood samples or from monitoring end-tidal CO_2 tension. Arterial oxygen tension (p_aO_2) was maintained at a level between 90 and 130 mmHg by adjusting the ratio of oxygen to medical air at ventilator setting. Blood glucose was also monitored and 1–2 ml infusion of 25% glucose solution was administered intravenously if blood glucose concentration fell below 4.5 mM.

Measurements started after a delay of 60 min following the completion of the surgical procedures to allow time for the physiological variables (HR, MAP, pCO_2, and p_aO_2) to stabilize. This delay was also sufficient to minimize any drift artifacts in the TR-NIRS measurements.[32] Piglets were placed in the prone position and a custom-made probe holder was strapped to the head to hold the emission and detection probes 2 cm apart, parasagittally, ~1.5 cm dorsal to the eyes directly in front of thermometer probe. Temperature was altered by placing plastic ice bags on the surface of the piglet's body until the brain temperature decreased to 31°C–32°C over ~3 to 4 h. For each experiment, the baseline count rate measured with the TR instrument was adjusted to 800 kHz to match the count rate used to measure the IRFs and was fixed for the remaining of the study. Tissue absorption coefficients were determined from reflectance data acquired continuously for 320 s at intervals of 10 s each. Each experiment was completed within 5 h. After the last measurement, the animals were sacrificed with intravenous potassium chloride ($1 - 2$ ml/kg) infusion. Thereafter, the brain was harvested and placed in paraformaldehyde for 24–48 h, and then transferred into a phosphate-buffered saline (PBS) solution for preservation. Excised brains were later paraffin embedded and cut into 5-μm-thick serial sections to verify the position of temperature probe and assess any potential bleeding caused by inserting the probe.

3 Data Analysis

A number of approaches have been developed to characterize the temperature dependency of water absorption spectrum, including Gaussian component, classical and inverse least squares, hybrid method, and principal components analysis (PCA).[20] In this study, TR-NIRS data were analyzed with the PCA method to predict tissue temperature. It has been shown that PCA can reduce random errors compared to the other methods and improve the fitting to the model.[20]

3.1 Temperature Fitting Algorithm

The workflow to predict temperature was as follows:

1. The calibration of pure water absorption spectrum against temperature was adapted from the work of Hollis et al.[20] As a first step, a data set containing many independent variables was decomposed into two sets of linear variables. In matrix notation, principal component regression (PCR) can be described as follows:

$$X = S \cdot P, \tag{1}$$

where the rows of data matrix X ($n \times m$) are the (n) pure water absorption spectra over (m) wavelengths at different temperatures at 0.1°C steps between 25°C and 45°C used in the calibration. The rows of P ($h \times m$) are the principal components of X, S ($n \times h$) contains the components scores, and (h) is the number of principal components used in the model. A MATLAB® program was written to determine the principal components of the mean-centered data set using an eigenvector decomposition technique.[33] The next stage of the PCR calibration was to establish a linear relationship between the components scores and temperature

$$t = S.v, \tag{2}$$

where t is the vector of the known calibration temperatures, v is the calibration vector relating the scores (S) to the temperature. Equations (1) and (2) provide the principal components (matrix P) and calibration vector (v) that are used to predict the temperature from any measured spectrum.

The extinction coefficients of the major tissue chromophores (H_2O, HbO_2, and Hb) were used to recover their concentrations from the absorption coefficients measured at the three wavelengths of the TR-NIRS instrument. Since the pure water absorption spectra were mean-centered for the PCR calibration, the mean water absorption coefficients from the calibration must also be included into the fitting

$$\mu_a(\lambda) = C_{H_2O} \cdot \left[\bar{\varepsilon}_{H_2O}(\lambda) + \sum_i S_i P_i(\lambda) \right] + \sum_{j=Hb,HbO_2} c_j \cdot \varepsilon_j(\lambda), \quad (3)$$

where $\mu_a(\lambda)$ is the absorption coefficient measured at wavelength λ, c_i is the concentration of the i'th chromophore, $\varepsilon_i(\lambda)$ is the extinction coefficient at λ, $\bar{\varepsilon}_{H_2O}$ is the the mean pure water absorption coefficient from the calibration at λ, S_i is the score of the i'th loading vector, and $P_i(\lambda)$ is a loading vector of the pure water at λ. In the first step, a least-square optimization algorithm (built around the function fminsearchbnd[34]) was used to extract the score of one pure water loading vector, i.e., PC, and concentrations of oxy- and deoxy-hemoglobin at baseline temperature by assuming a known water concentration of 95% and 85% for phantom and tissue experiments, respectively,[35,36] The optimization function was bound constrained, where bounds were applied to the recovered values to limit the search for oxy- and deoxy-hemoglobin concentrations to be in the range of 30–60 μM[37] and 5–25 μM,[38,39] respectively. Note that the extinction coefficients of pure water as a function of temperature as well as those of oxy- and deoxy-hemoglobin used in this study were taken from the literature.[40,41]

2. Predicted temperature was calculated by multiplying the scores of water loading vectors found in the previous step by the calibration vector

$$T_{predicted} = \sum_i S_{pc_i} \cdot v, \quad (4)$$

where v is the calibration vector relating the scores to the temperature obtained in step 1.

If the initial predicted temperature was different from the known temperature obtained by the thermometer at the beginning of the experiment, step 1 of Eq. (3) was altered to include a constant in order to find the corrected score related to the pure water loading vector corresponding to the initial temperature

$$\mu_a(\lambda) = C_{H_2O} \left[\bar{\varepsilon}_{H_2O}(\lambda) + \sum_i S_i P_i(\lambda) \right] + \sum_{i=Hb,HbO_2} c_i \varepsilon_i(\lambda) + \text{constant}. \quad (5)$$

3. The magnitude of the constant was determined using an iterative algorithm based on the criterion

$$\max(\text{diff}) \leq 0.5°C, \quad (6)$$

where

$$\text{diff} = (T_{predicted} - T_{thermometer})_{@initial\ temp}. \quad (7)$$

4. For subsequent temperature predictions, the chromophore fitting was repeated with the constant obtained from the correction for initial temperature, and then tissue temperature was computed as described in step 2.

3.2 Statistical Analysis

SPSS 17.0.0 (SPSS, Inc, Chicago, IL) was used for all statistical analyses. Normality of the distribution of the measurements was verified using Kolmogorov–Smirnov test. Physiological parameters between different temperatures were then analyzed using one-way analysis of variance (ANOVA). Correlations between the predicted temperatures against the temperatures measured by thermometry were analyzed using parametric linear regression. Finally, the degree of similarity between temperature measurements acquired with the two techniques was evaluated using a Bland–Altman plot.[42] Optical properties (μ_a and μ_s' at different temperatures were compared using a repeated measures two-way mixed ANOVA to determine statistical differences as a function of temperature for different wavelengths. Statistical significance was based on p-value < 0.05. All data are presented as mean $\pm$ standard deviation (SD) unless otherwise noted.

4 Results

Table 1 displays the temperature effects on absorption and reduced scattering coefficients for the tissue-mimicking phantoms. There was a statistically significant increase in absorption coefficient when temperature increases above 36°C at all three wavelengths. For a given temperature, the absorption coefficient was significantly lower at 760 nm than those at 810 and 830 nm, whereas the reduced scattering coefficient was significantly higher at 760 nm than that at 830 nm. No significant differences were found for reduced scattering coefficients between temperatures. Typical TPSFs acquired on the phantom and piglet's head at different temperatures are displayed in Fig. 2. For both sets of data, there was a reduction in the amplitude of the TPSFs as temperature decreased.

Figure 3(a) shows the plot of measured against predicted temperature of the tissue-mimicking phantom. The average slope, intercept, and R^2 value from the individual regression analyses were 1.01, −0.16°C, and 0.82. The Bland–Altman analysis [Fig. 3(b)] shows that the mean difference between the predicted and measured temperatures was 0.1°C. The 95% confidence interval of the difference between the two temperatures was 2.3°C to −2.1°C. Note that temperature prediction was not improved by inclusion of more than one water loading vector, i.e., more PCs (only one was used in this study).

Table 1 Absorption and reduced scattering coefficients of the tissue-mimicking phantom measured at four temperatures. Values are presented as mean ± SD.

Variable	λ (nm)	(32°C)	(34°C)	(36°C)	(38°C)
μ_a (mm^{-1})	830	$0.0142 \pm 0.005^\dagger$	$0.0147 \pm 0.005^\dagger$	$0.0152 \pm 0.006^\dagger$	$0.0175 \pm 0.007^{*\dagger}$
	810	$0.0127 \pm 0.004^\dagger$	$0.0131 \pm 0.005^\dagger$	$0.0134 \pm 0.005^\dagger$	$0.0155 \pm 0.005^{*\dagger}$
	760	0.0099 ± 0.003	0.0101 ± 0.003	0.0103 ± 0.003	$0.0118 \pm 0.003^*$
μ_s' (mm^{-1})	830	$1.99 \pm 0.12^\dagger$	$1.99 \pm 0.14^\dagger$	$1.97 \pm 0.15^\dagger$	$1.97 \pm 0.19^\dagger$
	810	2.08 ± 0.20	2.05 ± 0.21	2.06 ± 0.21	2.06 ± 0.26
	760	2.21 ± 0.19	2.21 ± 0.21	2.16 ± 0.17	2.17 ± 0.22

*A statistically significant ($P < 0.05$) difference compared to the baseline (32°C).
†A statistically significant ($P < 0.05$) difference compared to the value measured at 760 nm.
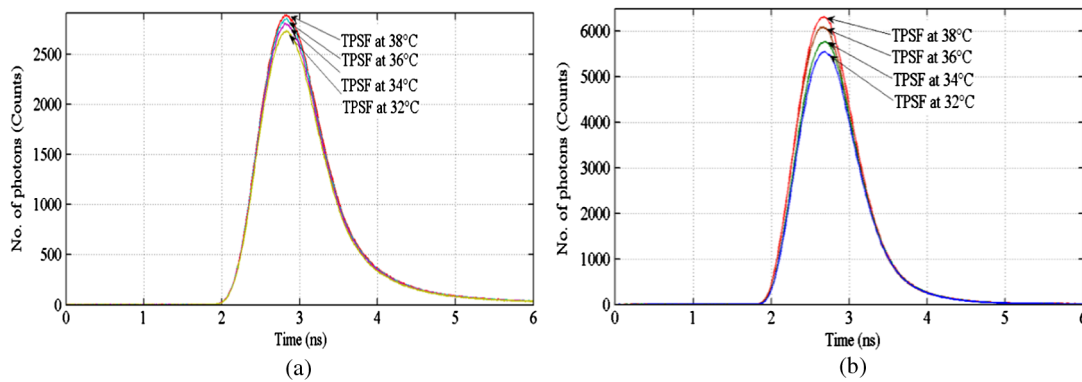

Fig. 2 A sample of raw data in showing distribution time of flight at different temperatures in (a) *in vitro* (tissue-mimicking phantoms) and (b) *in vivo* (newborn piglets brain).
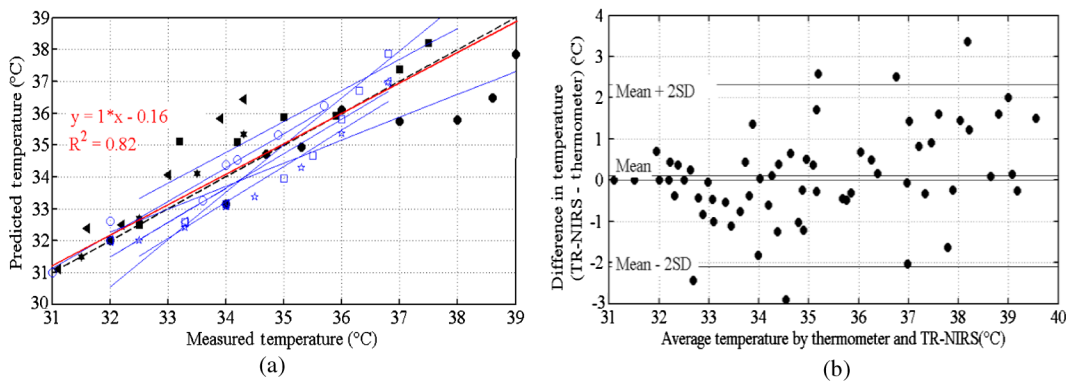

Fig. 3 (a) Correlation plot comparing temperature of the tissue-mimicking phantom calculated by TR-NIRS against temperature measured with a thermometer (labeled predicted temperature and measured temperature, respectively). Each symbol type represents data from one of the seven tissue-mimicking phantoms. The solid line represents the average of all individual linear regression lines and the dotted line indicates the line of identity (slope = 1). (b) Bland–Altman plot comparing predicted and measured temperature. The dotted line and dash-dotted lines show the mean and the 95% confidence limits of the difference (mean ± 2 SD) between the two temperature measurements.

Table 2 displays a summary of the measured physiological parameters of the piglets at the different brain temperatures. There was a statistically significant decrease in HR and P_aO_2 when temperature dropped to 34°C and lower. Furthermore, analysis of the brain tissue sections revealed no gross hemorrhages caused by insertion of the thermometer probe into the brain.

Table 3 provides the measured μ_a and μ_s' of the piglet brain at three wavelengths and at different temperatures. The absorption coefficient was higher at 830 nm than at 810 and 760 nm

Table 2 Physiological parameters measured at different brain temperatures. Values are mean ± SD.

	(38°C)	(36°C)	(34°C)	(32°C)
MAP (mmHg)	42 ± 5	41 ± 4	40 ± 4	38 ± 4
HR (bpm)	139 ± 10	125 ± 14	109 ± 11[*]	94 ± 13[*]
pH	7.4 ± 0.01	7.4 ± 0.02	7.4 ± 0.01	7.5 ± 0.1
p_aCO_2 (mmHg)	39 ± 1	38 ± 2	40 ± 1	38 ± 1
p_aO_2 (mmHg)	122 ± 15	93 ± 7	90 ± 17[*]	75 ± 17[*]
Hb (μmol/L)	24.9 ± 9.2	25.4 ± 10.8	25.2 ± 11.2	26.7 ± 11.1
HbO$_2$ (μmol/L)	63.4 ± 20.9	62.9 ± 20.6	63.3 ± 19.9	61.5 ± 20.2
tHb (μmol/L)	88.4 ± 22.3	88.3 ± 23.1	88.7 ± 22	88.9 ± 21.8

MAP=mean arterial blood pressure; HR = heart rate; tHb = total hemoglobin; Hb = Deoxy-hemoglobin; HbO$_2$ = Oxy-hemoglobin.
[*]A statistically significant ($P < 0.05$) difference compared to the baseline (38°C).

Table 3 Absorption and reduced scattering coefficients measured at four temperatures in the newborn piglet brain. Values are mean ± SD.

Variable	λ (nm)	(38°C)	(36°C)	(34°C)	(32°C)
μ_a (mm^{-1})	830	0.0240 ± 0.005[*]	0.0242 ± 0.005[*]	0.0225 ± 0.005[*]	0.0177 ± 0.001
	810	0.0214 ± 0.003	0.0219 ± 0.004	0.0204 ± 0.003	0.0168 ± 0.002
	760	0.0214 ± 0.002	0.0223 ± 0.003	0.0212 ± 0.004	0.0173 ± 0.002
μ_s' (mm^{-1})	830	0.68 ± 0.08[*]	0.67 ± 0.07[*]	0.67 ± 008[*]	0.67 ± 0.05[*]
	810	0.74 ± 0.10	0.74 ± 0.08	0.73 ± 0.11	0.80 ± 0.05
	760	0.79 ± 0.13	0.78 ± 0.11	0.73 ± 0.13	0.81 ± 0.12

[*]A statistically significant ($P < 0.05$) difference compared to the value measured at 760 nm.

and, as expected, the reduced scattering coefficient decreased as wavelength increased.[43]

Figure 4(a) shows the correlation plot of predicted brain temperature calculated by TR-NIRS versus the temperature measured with the thermometer. Results from regression analysis

for each piglet as well as the average of all experiments are shown. The average slope, intercept, and R^2 value from the individual regression analyses were 1.1, −1.6°C, and 0.66, respectively. The Bland–Altman analysis in Fig. 4(b) shows that the mean difference between the predicted and measured
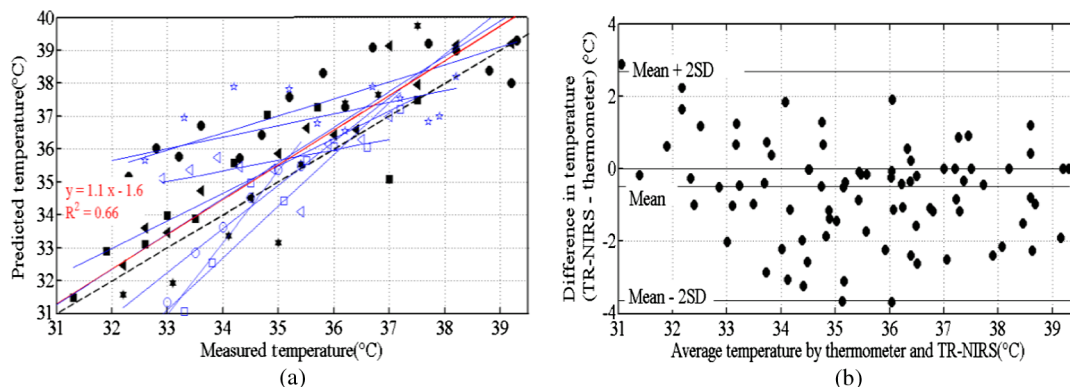

Fig. 4 (a) Correlation plot comparing temperature in the piglet brain calculated by TR-NIRS against temperature measured with a thermometer (labeled predicted temperature and measured temperature, respectively). Each symbol type represents data from one of eight piglets. The solid line represents the average of all individual linear regression lines and the dotted line indicates the line of identity (slope = 1). (b) Bland–Altman plot comparing predicted and measured temperatures. The dotted line shows the mean difference and dash-dotted lines show the limits of agreement (mean ± 2 SD) between the two temperature measurements.

temperatures was 0.5℃. The 95% confidence interval of the difference between the two temperatures was 2.7℃ to −3.6℃.

5 Discussion

We investigated the ability of TR-NIRS to measure temperature in tissue-mimicking phantoms and newborn piglets' brain using the temperature dependence of water absorption features at 740 and 840 nm. The TR-NIRS temperature measurements were based on subtle changes in the NIR water absorption with the following assumptions. First, the concentration of water in the brain was assumed to be 85% in order to calculate the score of one pure water loading vector as well as cerebral hemoglobin concentrations. Second, the initial tissue temperature was known from thermometry to find the corrected score related to the pure water loading vector. Third, to determine optical properties from changes in light absorption caused by cooling, the scaling factor and μ_s' were set to their baseline values and only μ_a was used as fitting parameter. This approach has been shown to improve the stability of the fitting procedure by limiting the number of fitting parameters as well as reducing cross talk between parameters.[20,27] Including the scaling factor or μ_s' as a fitting parameter resulted in a weaker correlation between the TR-NIRS and thermometer measurements for phantom experiments (R^2 from 0.68 to 0.57 respectively; data not shown). Furthermore, we assumed that the molar extinction coefficient of oxy- and deoxy- hemoglobin was constant over the temperature range of 39–31℃. Temperature-dependent changes of hemoglobin NIR absorption spectra have been investigated[44]; and these changes are relatively small compared to the change in the water spectrum. Specifically, the amplitude of the spectra of Hb and HbO$_2$ decreased by $0.15\% - 0.18\%℃^{-1}$ and $0.05\%℃^{-1}$, respectively, when the temperature was increased from 20℃ to 40℃. Likewise, the amplitude shift was only 0.08 nm℃$^{-1}$ and 0.15 nm℃$^{-1}$ from 700 to 1100 nm for Hb and HbO$_2$, respectively.[44]

The proposed TR-NIRS thermometry was tested against direct thermometer measurement in tissue-mimicking phantoms. Results demonstrated that TR-NIRS was sensitive to temperature changes via changes in the water absorption coefficient and could accurately measure the temperature of tissue-mimicking phantoms. A strong correlation ($R^2 = 0.82$) between the predicted temperatures calculated from TR-NIRS and thermometer measurements was observed with a slope of 1.01, indicating the equivalency between the optical and thermometer measurements over the range of 33℃–38℃. The average difference between the TR-NIRS prediction and the measured temperature was $0.15℃ \pm 1.1℃$.

For the *in vivo* temperature measurement, we used piglets because they are commonly used as an animal model of human newborn neurophysiology[45] and signal contamination from the extracerebral tissue is relatively small, which enables the measured TPSFs to be modeled by the solution to the diffusion equation for a homogeneous semi-infinite geometry.[46] A good correlation between the thermometer measured and TR-NIRS predicted temperatures was obtained ($R^2 = 0.66$) with a slope of 1.1 over the range of 31℃–39℃. The higher variability observed in the *in vivo* temperature predictions may be due to physiological instabilities, such as thermoregulatory responses to a decline in body temperature, effects of cold-induced vasoconstriction, reduction of mean arterial pressure, and cardiac output.[47] Vasoconstriction during hypothermia[48] will decrease the cerebral blood volume, and hence cause a reduction in μ_a. There are other potential sources of errors that could contribute to the discrepancies between the TR-NIRS and thermometer measurements. One source of error could be inaccurate estimates of the optical properties caused by errors in the measured IRF.[28] However, the IRF was measured using a procedure that has been shown to provide accurate estimate of tissue optical properties.[28,46] Another potential source of error is employing the pure water absorption spectrum and parameters associated with the temperature response that were used for fitting tissue temperature, i.e., the calibration vector and PCs. The difference in absorption spectrum between tissue and pure water is due to bound water within tissue.[49] In our calculation, the chromophore fitting was performed with the loading vectors obtained from the PCA of pure water absorption spectrum rather than that of "tissue water," which resulted in the predicted temperature either underestimating or overestimating the thermometer temperature. As such, a correction was performed using a constant value [Eq. (3)] to make the predicted temperature as close as possible to the true initial temperature, which was known from the thermometer.

In principle, the accuracy of the temperature prediction can be improved by increasing the number of wavelengths used to sample the tissue absorption spectrum, which would result in improved chromophore quantification. This can be achieved by increasing the number of lasers or using a pulsed supercontinuum light source to eliminate the need for assuming a known water concentration. Improved spectral coverage can also be obtained by combination of TR and broadband CW spectroscopy, whereas most of the wavelength coverage would be provided by the hyperspectral CW measurement, and the TR data would provide μ_a and μ_s' at a few selected NIR wavelengths. Coefficients of absorption and reduced scattering derived from the TR data would, then, be used to calibrate the intensity of the CW measurements to estimate optical properties at all wavelengths in the spectral window of interest.[50,51]

The main drawbacks of TR-NIRS are cost and instrument complexity; however, new technical breakthroughs are promising improved instrumentation and eventually reduced cost.[52,53] Despite cost and complexity, TR-NIRS has a number of advantages compared to steady-state and frequency domain NIRS, specially the ability to distinguish early from late-arriving photons. Since photons with extended time-of-flight have a higher probability of probing deeper tissue, TR-NIRS enables discrimination of superficial changes from deep tissue absorption.[54] This ability can be exploited to improve the sensitivity of the TR-NIRS thermometry to deep brain tissue, particularly in adults, wherein the superficial layers of the head have substantial contribution to the measurements.

In conclusion, we have demonstrated a method of monitoring tissue temperature noninvasively using the temperature response of water absorption peaks in the NIR spectral region. The results from tissue-mimicking phantoms show a strong correlation ($R^2 = 0.82$) between the TR-NIRS and thermometer measurements. We also showed the potential of the TR-NIRS to measure temperature *in vivo* in an animal model of the newborn. Since the method is safe and measurements can be obtained at the bedside in only a few minutes, it is believed that this technique could assist in monitoring brain temperature in the neonate during hypothermia therapy.

References

1. E. M. Moore et al., "Therapeutic hypothermia: benefits, mechanisms and potential clinical applications in neurological, cardiac and kidney injury," *Injury* **42**(9), 843–54 (2011).
2. J. W. Lampe and L. B. Becker, "State of the art in therapeutic hypothermia," *Annu. Rev. Med.* **62**, 79–93 (2011).
3. M. W. Quinn and P. F. Munyard, "Treatment of asphyxiated newborns with moderate hypothermia in routine clinical practice: how cooling is managed in the UK outside a clinical trial," *Arch Dis Child Fetal Neonatal Ed.* **95**(2), F152 (2010).
4. E. Suehiro et al., "Significance of differences between brain temperature and core temperature (delta T) during mild hypothermia in patients with diffuse axonal injury," *Neurol Med Chir (Tokyo)* **51**(8), 551–555 (2011).
5. C. Childs and K. W. Lunn, "Clinical review: brain-body temperature differences in adults with severe traumatic brain injury," *Crit. Care* **17**(2), 222 (2013).
6. S. Sarkar and J. D. Barks, "Systemic complications and hypothermia," *Semin. Fetal Neonatal Med.* **15**(5), 270–275 (2010).
7. D. Straus, V. Prasad, and L. Munoz, "Selective therapeutic hypothermia: a review of invasive and noninvasive techniques," *Arq Neuropsiquiatr* **69**(6), 981–987 (2011).
8. M. S. Tsai et al., "Rapid head cooling initiated coincident with cardiopulmonary resuscitation improves success of defibrillation and post-resuscitation myocardial function in a porcine model of prolonged cardiac arrest," *J. Am. Coll. Cardiol.* **51**(20), 1988–1990 (2008).
9. D. Kirk et al., "Infra-red thermometry: the reliability of tympanic and temporal artery readings for predicting brain temperature after severe traumatic brain injury," *Crit. Care* **13**(3), R81 (2009).
10. C. Childs, R. Harrison, and C. Hodkinson, "Tympanic membrane temperature as a measure of core temperature," *Arch. Dis. Child* **80**(3), 262–266 (1999).
11. J. Shin et al., "Core temperature measurement in therapeutic hypothermia according to different phases: comparison of bladder, rectal, and tympanic versus pulmonary artery methods," *Resuscitation* **84**(6), 810–817 (2013).
12. Z. Mariak et al., "The relationship between directly measured human cerebral and tympanic temperatures during changes in brain temperatures," *Eur. J. Appl. Physiol. Occup. Physiol.* **69**(6), 545–549 (1994).
13. J. Weis et al., "Phase-difference and spectroscopic imaging for monitoring of human brain temperature during cooling," *Magn. Reson. Imaging* **30**(10), 1505–1515 (2012).
14. M. Fatar et al., "Brain temperature during 340-kHz pulsed ultrasound insonation: a safety study for sonothrombolysis," *Stroke* **37**(7), 1883–1887 (2006).
15. K. T. Karathanasis et al., "Noninvasive focused monitoring and irradiation of head tissue phantoms at microwave frequencies," *IEEE Trans. Inf. Technol. Biomed.* **14**(3), 657–663 (2010).
16. A. Dittmar et al., "A non invasive wearable sensor for the measurement of brain temperature," in *Conf. Proc. IEEE Eng. Med. Biol. Soc.*, Vol. 1, pp. 900–902 (2006).
17. D. Brajkovic and M. B. Ducharme, "Confounding factors in the use of the zero-heat-flow method for non-invasive muscle temperature measurement," *Eur. J. Appl. Physiol.* **94**(4), 386–391 (2005).
18. K. R. Foster and E. A. Cheever, "Microwave radiometry in biomedicine: a reappraisal," *Bioelectromagnetics* **13**(6), 567–579 (1992).
19. A. Levick, D. Land, and J. Hand, "Validation of microwave radiometry for measuring the internal temperature profile of human tissue," *Meas. Sci. Technol.* **22**(6), 065801 (2011).
20. V. Hollis, "Non-invasive monitoring of brain tissue temperature by near-infrared spectroscopy," PhD Thesis, Univ. College London (2002).
21. V. Langford, "Temperature dependence of the visible-near-infrared absorption spectrum of liquid water," *J. Phys. Chem. A* **105**(39), 8916–8921 (2001).
22. J. Kelly, "Tissue temperature by near-infrared spectroscopy," *Proc. SPIE* **2389**, 818–828 (1995).
23. S. H. Chung et al., "Non-invasive tissue temperature measurements based on quantitative diffuse optical spectroscopy (DOS) of water," *Phys. Med. Biol.* **55**(13), 3753–3765 (2010).
24. J. Selb et al., "Improved sensitivity to cerebral hemodynamics during brain activation with a time-gated optical system: analytical model and experimental validation," *J. Biomed. Opt.* **10**(1), 011013 (2005).
25. N. Okui and E. Okada, "Wavelength dependence of crosstalk in dual-wavelength measurement of oxy- and deoxy-hemoglobin," *J. Biomed. Opt.* **10**(1), 011015 (2005).
26. R. H. Ossoff, "Implementing the ANSI Z 136.3 laser safety standard in the medical environment," *Otolaryngol. Head Neck Surg.* **94**(4), 525–528 (1986).
27. V. Ntziachristos and B. Chance, "Accuracy limits in the determination of absolute optical properties using time-resolved NIR spectroscopy," *Med. Phys.* **28**(6), 1115–1124 (2001).
28. A. Liebert et al., "Fiber dispersion in time domain measurements compromising the accuracy of determination of optical properties of strongly scattering media," *J Biomed. Opt.* **8**(3), 512–516 (2003).
29. A. Kienle and M.S. Patterson, "Improved solutions of the steady-state and the time-resolved diffusion equations for reflectance from a semi-infinite turbid medium," *J. Opt. Soc. Am. A Opt. Image Sci. Vis.* **14**(1), 246–254 (1997).
30. E. Alerstam, S. Andersson-Engels, and T. Svensson, "Improved accuracy in time-resolved diffuse reflectance spectroscopy," *Opt. Express* **16**(14), 10440–10454 (2008).
31. W. Becker, *Advanced Time-Correlated Single Photon Counting Technique*, Springer, New York (2005).
32. M. Diop et al., "Bedside monitoring of absolute cerebral blood flow by time-resolved NIRS," *Proc. SPIE* **7555**, 75550Z (2010).
33. J. Shlens, A Tutorial on Principal Component Analysis, Institute for Nonlinear Science, San Diego (2005).
34. J. D'Errico, "fminsearchbnd, fminsearchcon—file exchange—matlab central [online]," http://www.mathworks.com/matlabcentral/fileexchange/8277-fminsearchbnd, 6 February 2012 (20 January 2014).
35. D. R. White et al., "The composition of body tissues (II). Fetus to young adult," *Br. J. Radiol.* **64**(758), 149–159 (1991).
36. C. E. Cooper et al., "The noninvasive measurement of absolute cerebral deoxyhemoglobin concentration and mean optical path length in the neonatal brain by second derivative near infrared spectroscopy," *Pediatr. Res.* **39**(1), 32–38 (1996).
37. S. Fantini et al., "Non-invasive optical mapping of the piglet brain in real time," *Opt. Express* **4**(8), 308–314 (1999).
38. K. M. Tichauer et al., "Using near-infrared spectroscopy to measure cerebral metabolic rate of oxygen under multiple levels of arterial oxygenation in piglets," *J. Appl. Physiol.* **109**(3), 878–885 (2010).
39. S. J. Matcher and C. E. Cooper, "Absolute quantification of deoxyhaemoglobin concentration in tissue near infrared spectroscopy," *Phys. Med. Biol.* **39**(8), 1295–1312 (1994).
40. S. J. Matcher et al., "Performance comparison of several published tissue near-infrared spectroscopy algorithms," *Anal. Biochem.* **227**(1), 54–68 (1995).
41. Biomedical optics laboratory, University of London, "Specific extinction spectra of tissue chromophores," Available from: http://www.medphys.ucl.ac.uk/research/borl/research/NIR_topics/spectra/spectra.htm. Available from: http://www.medphys.ucl.ac.uk/research/borl/research/NIR_topics/spectra/spectra.htm (September 2009).
42. J. M. Bland and D.G. Altman, "Statistical methods for assessing agreement between two methods of clinical measurement," *Lancet* **327**(8476), 307–310 (1986).
43. Q. Fu and W. Sun, "Mie theory for light scattering by a spherical particle in an absorbing medium," *Appl. Opt.* **40**(9), 1354–1361 (2001).
44. R. Sfareni et al., "Near infrared absorption spectra of human deoxy- and oxyhaemoglobin in the temperature range 20–40 degrees C," *Biochim. Biophys. Acta.* **1340**(2), 165–169 (1997).
45. T. Roohey, T. N. Raju, and A. N. Moustogiannis, "Animal models for the study of perinatal hypoxic-ischemic encephalopathy: a critical analysis," *Early Hum. Dev.* **47**(2), 115–146 (1997).
46. M. Diop et al., "Comparison of time-resolved and continuous-wave near-infrared techniques for measuring cerebral blood flow in piglets," *J. Biomed. Opt.* **15**(5), 057004 (2010).
47. G. Cavallaro et al., "Heart rate and arterial pressure changes during whole-body deep hypothermia," *ISRN Pediatr.* **2013**, 140213 (2013).

48. E. Satinoff, "Behavioral thermoregulation in response to local cooling of the rat brain," *Am. J. Physiol.* **206**, 1389–1394 (1964).

49. S. H. Chung et al., "In vivo water state measurements in breast cancer using broadband diffuse optical spectroscopy," *Phys. Med. Biol.* **53**(23), 6713–6727 (2008).

50. F. Bevilacqua et al., "Broadband absorption spectroscopy in turbid media by combined frequency-domain and steady-state methods," *Appl. Opt.* **39**(34), 6498–6507 (2000).

51. W. Cai, M. Xu, and R. R. Alfano, "Analytical form of the particle distribution based on the cumulant solution of the elastic Boltzmann transport equation," *Phys. Rev. E. Stat. Nonlin. Soft. Matter. Phys.* **71**(4 Pt 1), 041202 (2005).

52. J. Arlt et al., "A study of pile-up in integrated time-correlated single photon counting systems," *Rev. Sci. Instrum.* **84**(10), 103105 (2013).

53. D. Tyndall et al., "A high-throughput time-resolved mini-silicon photo-multiplier with embedded fluorescence lifetime estimation in 0.13 mum CMOS," *IEEE Trans. Biomed. Circuits Syst.* **6**(6), 562–570 (2012).

54. M. Diop and K. St Lawrence, "Improving the depth sensitivity of time-resolved measurements by extracting the distribution of times-of-flight," *Biomed. Opt. Express* **4**(3), 447–459 (2013).

Biographies of the authors are not available.